International Journal of Modern Physics A

Study the production of identified charged hadrons in Au+Au collisions at $\sqrt{s_{NN}}$ = 54.4 GeV using the STAR detector

Arushi Dhamija (for the STAR Collaboration)
Department of Physics, Panjab University, Chandigarh-160014, India
arushidhamija507@gmail.com

Received Day Month Year
Revised Day Month Year

The properties of Quark-Gluon Plasma (QGP) and complex dynamics of multi-scale processes in Quantum Chromodynamics (QCD) can be studied in relativistic heavy-ion collision experiments by analyzing the final state particles. In this proceedings, we present our comprehensive findings derived from the measurements of $\pi^{\pm}$, $K^{\pm}$, p, and $\bar{p}$ production in Au+Au collisions at $\sqrt{s_{NN}}$ = 54.4 GeV at mid-rapidity ($|y| < 0.1$). The data were collected during the Beam Energy Scan (BES-II) program of Relativistic Heavy Ion Collider (RHIC) using the Solenoidal Tracker at RHIC (STAR) detector. Moreover, we determine the kinetic freeze-out parameters, unraveling crucial insights into the lifespan of the fireball.

Keywords: Heavy-ion collisions; QGP; STAR.

1. Introduction

Colliding heavy ions at high energies is a way to create and study the QGP on the earth. The QCD phase diagram is usually plotted as a function of temperature (T) and the baryon chemical potential (μ_B). Lattice QCD calculations indicate that the phase diagram shows a transition from the partonic degrees of freedom to a phase where the relevant degrees of freedom are hadronic in nature.[1–4] As suggested by several QCD-based models, high μ_B region corresponds to the first order phase transition while at very low μ_B the transition is a rapid crossover.[1–4] The point where the first order phase transition ends, the transition begins to crossover, and the phase boundaries cease to exist is called the QCD critical point.[1–4] Due to color confinement, the quarks and gluons cannot be directly observed during experiments as they are liberated for a very short period of time. The exclusive method to study the QGP is by analyzing the particles that emerge from the freeze-out in the final state.

The Beam Energy Scan (BES) program at RHIC aims to search for the QCD phase boundary and the conjectured QCD critical point by varying the collision energies. To identify signs of the QCD critical point and phase boundary, understanding a wide (T, μ_B) region in the phase diagram is crucial. This understanding

can be derived through analyzing the spectra and yields of the generated particles. In addition, the integrated particle yields, particle ratios and freeze-out parameters provide insights into the particle production mechanisms, evolution and the change in the behavior of the system formed in heavy-ion collisions as a function of collision energy.[5] The STAR experiment conducted the BES-I program from 2010 - 2014 with Au+Au data sets in the centre-of-mass energy of 62.4, 39, 27, 19.6, 11.5 and 7.7 GeV. As an extension to the BES-I program, in 2017, the BES-II program was introduced which included both the fixed-target mode and the collider mode with much larger statistics.

2. Data set and Particle Identification

2.1. *Data set*

The results presented in this contribution are based on the datasets of Au+Au collisions at $\sqrt{s_{NN}} = 54.4$ GeV taken in 2017. The detectors that played a major role in the particle identification were the Time Projection Chamber (TPC) and the Time Of Flight (TOF) detectors. For optimization of the data, selection criteria were applied which included event and track selection cuts. The data set was divided into nine centrality classes, 0-5% (central), 5-10%, 10-20%, 20-30%, 30-40%, 40-50%, 50-60%, 60-70% and 70-80% (peripheral).

2.2. *Particle Identification*

Particle identification for low momentum is accomplished using the TPC detector by measuring the average ionization energy loss per unit path length $\langle dE/dx \rangle$. To identify the particles, a z-variable is constructed which is defined as

$$z_X = ln\left(\frac{\langle dE/dx \rangle}{\langle dE/dx \rangle_X^B}\right) \tag{1}$$

where X is the particle type and B corresponds to the Bichsel function expected value. The z-distributions are fitted with multi-gaussian to extract the raw yield of the particle of interest at a given p_T.[5] At low p_T the distributions of pions, kaons, and protons are well separated, however, at higher p_T they start to overlap. TPC is used for particle identification at low momentum from 0.2 to 0.7 GeV/c (0.4 to 0.9 GeV/c) for pions and kaons (protons and anti-protons).

To identify the particles at high momentum, we use the time-of-flight information. The raw yields from TOF are obtained using the variable mass-square (m^2), given by

$$m^2 = p^2\left(\frac{c^2T^2}{L^2} - 1\right), \tag{2}$$

where p is the momentum, T is time-of-travel, L is the path length. TOF is used for particle identification from $p_T = 0.7$ to 2 GeV/c (0.9 to 2.0 GeV/c) for pions and kaons (protons and anti-protons).

3. Results

3.1. *Transverse momentum spectra*

The transverse momentum spectra provide important insights into the various aspects of the system, such as thermalization, particle production, collective flow behavior, as well as the dynamics and properties of the produced particles.[5] Figure 1 shows the transverse momentum spectra of the identified charged hadrons $\pi^{\pm}$, $K^{\pm}$, p and $\bar{p}$ in nine centrality classes.

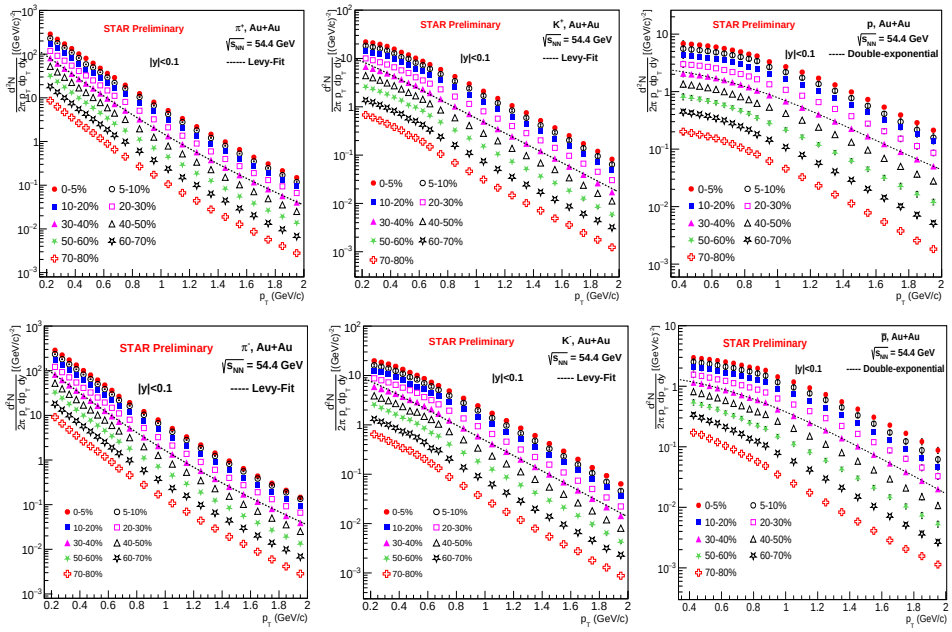

Fig. 1. Transverse mometum spectra of π^+, π^-, K^+, K^-, p, and $\bar{p}$ measured in mid-rapidity $|y| < 0.1$ in Au+Au collisions at $\sqrt{s_{NN}} = 54.4$ GeV in STAR. The curves represent the Levy-Tsallis function for $\pi^{\pm}$ and $K^{\pm}$ and double exponential for p and $\bar{p}$

3.2. *Integrated particle yields*

The obtained spectra were fitted with the Levy-Tsallis function for pions and kaons, and with the double exponential function for protons and anti-protons. Functional extrapolation was employed to estimate particle yield in the unmeasured p_T range, while the measured data points were utilized to estimate the particle yield within the measured p_T. The obtained yields were divided by 0.5 * number of participating nucleons ($\langle N_{part} \rangle$) in each centrality class, allowing for a normalized comparison between different centrality levels. Figure 2 shows the normalised yields for π^+, π^-, K^+, K^-, p, and $\bar{p}$. The normalized yield for π^+, π^-, K^+ and K^- show clear energy and centrality dependence. The normalized yield for these particles increases with

the increasing energy. The proton yield is maximum at $\sqrt{s_{NN}} = 7.7$ GeV and then decreases until 39 GeV, after which it slightly increases up to 200 GeV. The significant proton yield at $\sqrt{s_{NN}} = 7.7$ GeV can be attributed to the baryon stopping at lower energies, whereas as the energy increases, pair production dominates. The normalized yield for $\bar{p}$ shows weak centrality dependence but clear energy dependence.

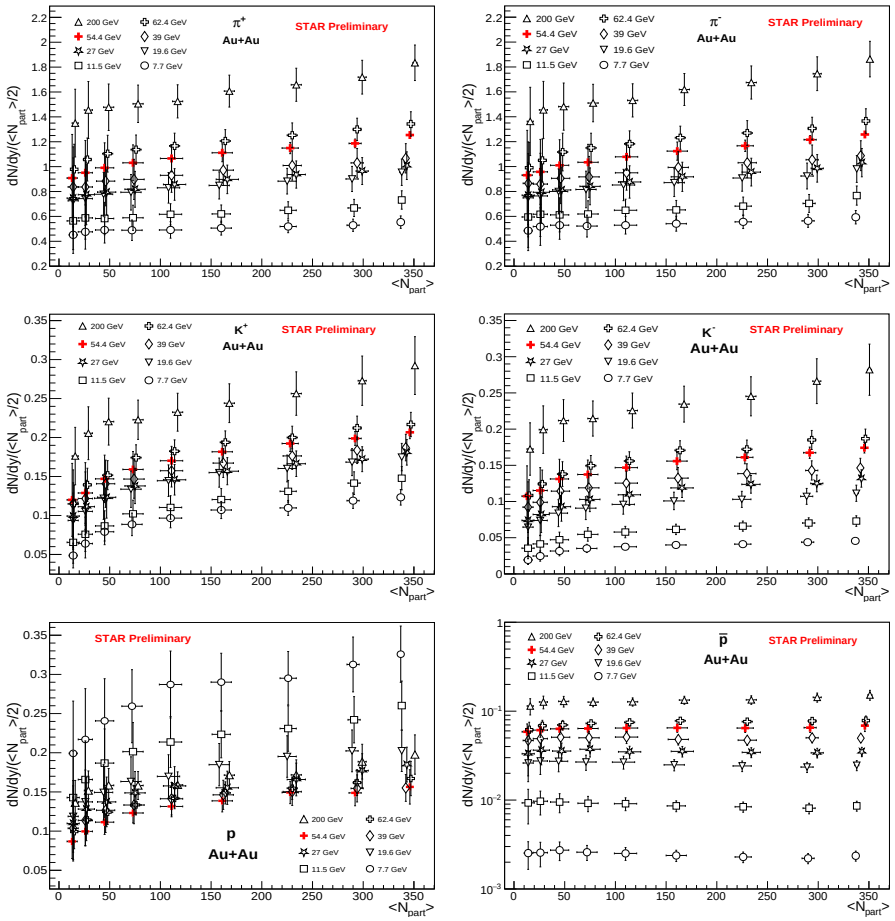

Fig. 2. The integrated particle yield of π^+, π^-, K^+, K^-, p and $\bar{p}$) as a function of $\langle N_{part} \rangle$ for Au+Au collisions at $\sqrt{s_{NN}} = 54.4$ GeV in STAR. The results are shown in comparison with various Au+Au collisions at other energies from STAR .[5,6] The statistical and systematic uncertainties are added in quadrature and are shown as vertical bars.

3.3. *Particle ratios*

3.3.1. *Centrality dependence*

Figure 3 shows the various anti-particle to particle ratios (π^-/π^+, K^-/K^+, and $\bar{p}/p$) as a function of collision centrality. The π^-/π^+ ratio is close to unity for all the centralities at Au+Au $\sqrt{s_{NN}} = 54.4$ GeV. K^-/K^+ ratio shows little centrality dependence for all the energies. The $\bar{p}/p$ ratio increases from central to peripheral collisions which reflects high baryon stopping in most central collisions as compared to the most peripheral collisions.

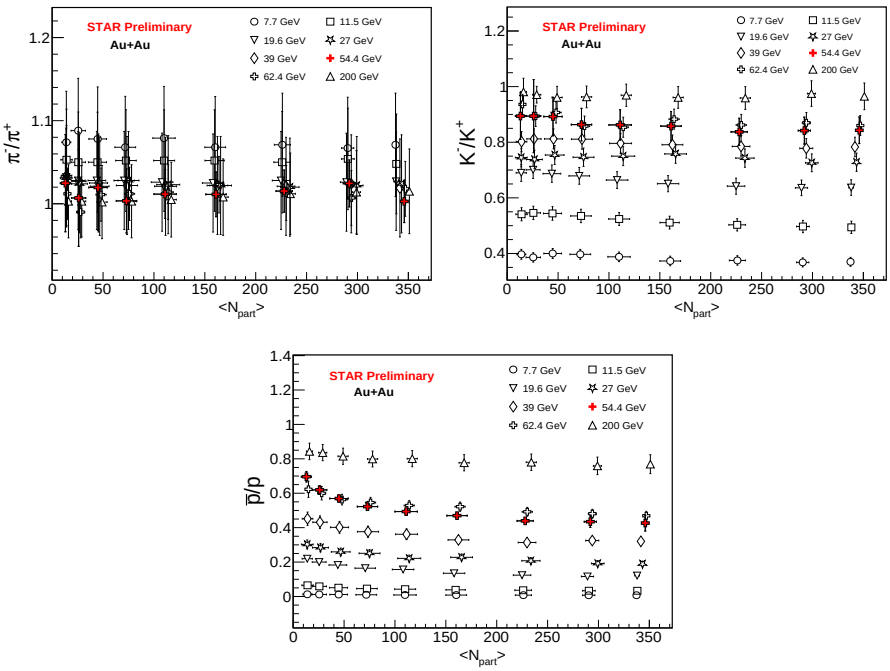

Fig. 3. The anti-particle to particle ratio of π^-/π^+, K^-/K^+,and $\bar{p}$/p as a function of $\langle N_{part}\rangle$ for Au+Au collisions at $\sqrt{s_{NN}} = 54.4$ GeV in STAR. The results are shown in comparison with various Au+Au collisions at other energies from STAR .[5,6] The statistical and systematic uncertainties are added in quadrature and are shown as vertical bars.

Figure 4 shows the centrality dependence of the mixed ratios (K^-/π^-, K^+/π^+, p/π^+, and $\bar{p}/\pi^-$). The results are compared with the other results for STAR BES.[5,6] K^+/π^+ ratio is maximum at $\sqrt{s_{NN}} = 7.7$ GeV and then decreases with the increasing energy. This might be due to the dominance of associated production due to large baryon stopping at low energies. The K^-/π^- ratio increases with the increasing energy and centrality. It is also observed that the variation from central to peripheral collisions is the most at lower energies, and the extent of variation between centralities decreases with the increasing energy. The p/π^+ ratio decreases with the

increasing energy and is largest at $\sqrt{s_{NN}}$ = 7.7 GeV, which is a consequence of large baryon stopping at lower energies. The ratio increases from peripheral to central collisions for lower energies while the significant variation between centralities is not observed at higher energies. The $\bar{p}/\pi^-$ increases with the increasing energy and shows weak centrality dependence.

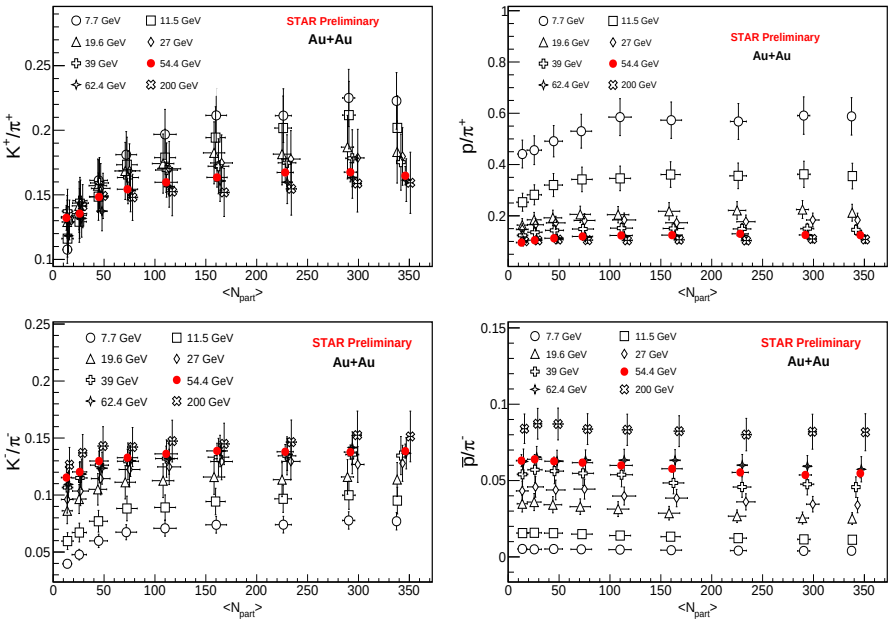

Fig. 4. The mixed particle ratios of K^+/π^+, p/π^+, K^-/π^-, and $\bar{p}/\pi^-$ as a function of $\langle N_{part}\rangle$ for Au+Au collisions at $\sqrt{s_{NN}}$ = 54.4 GeV in STAR. The results are shown in comparison with various Au+Au collisions at other energies from STAR .[5,6] The statistical and systematic uncertainties are added in quadrature and are shown as vertical bars.

3.3.2. *Energy dependence*

Figure 5 shows the anti-particle to particle ratio as a function of beam energy. The π^-/π^+ ratio is close to unity at Au+Au $\sqrt{s_{NN}}$ = 54.4 GeV. The lowest energy $\sqrt{s_{NN}}$ = 7.7 GeV, has π^-/π^+ ratio greater than 1, due to isospin and significant contributions from the resonance decays (such as Δ baryons) .[5] K^-/K^+ ratio increases with the increase in energy. The $\bar{p}/p$ ratio increases from with the increasing energy which reflects high baryon density due to baryon stopping at lower energies.

3.4. *Kinetic freeze-out*

The kinetic freeze-out parameters were obtained using the Blast-wave model.[14,15] The transverse momentum spectra of $\pi^{\pm}$, $K^{\pm}$, p and $\bar{p}$ were fitted simultaneously

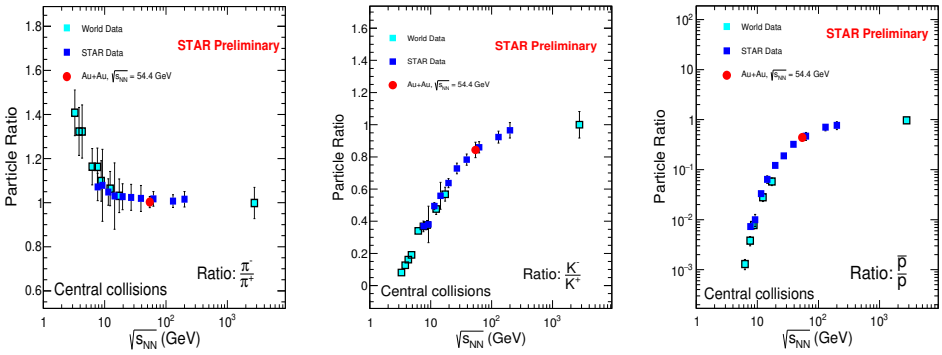

Fig. 5. The anti-particle to particle ratio of π^-/π^+, K^-/K^+,and $\bar{p}/p$ as a function of energy for Au+Au collisions at $\sqrt{s_{NN}} = 54.4$ GeV in STAR. The results are shown in comparison with various Au+Au collisions at other energies from STAR .[5–13] The statistical and systematic uncertainties are added in quadrature and are shown as vertical bars.

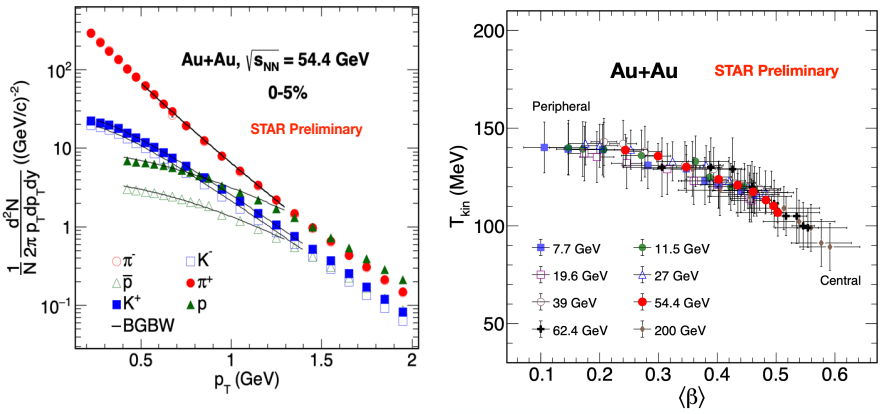

Fig. 6. The left figure shows the simultaneous BW fit to the $\pi^{\pm}$, $K^{\pm}$, p and $\bar{p}$ transverse momentum spectra for Au+Au collisions at $\sqrt{s_{NN}} = 54.4$ GeV in STAR in 0-5% centrality. The right figure shows the variation of T_{kin} and $\langle\beta\rangle$ in all centralities with other energies.[5,6] The statistical and systematic uncertainties are added in quadrature and are shown as vertical bars.

to extract the kinetic freeze-out temperature (T_{kin}) and average transverse radial flow velocity ($\langle\beta\rangle$). The transverse momentum distribution of the particles can be described by:

$$\frac{dN}{p_T dp_T} \propto \int_0^R r dr m_T I_0\left(\frac{p_T sinh\rho(r)}{T_{kin}}\right) \times K_1\left(m_T cosh\frac{\rho(r)}{T_{kin}}\right) \tag{3}$$

where $m_T = \sqrt{p_T^2 + m^2}$, m being the mass of the hadron, $\rho(r) = \tanh^{-1}\beta$, I_0 and K_1 are modified Bessel functions. We use radial flow velocity of the form $\beta = \beta_S(\mathrm{r/R})^n$, where β_S is the surface velocity and r/R is the relative radial position in

the thermal source and n is the exponent of flow velocity profile. Average radial flow is obtained as $\langle\beta\rangle = \frac{2}{2+n}\beta_S$. Figure 6 shows the simultaneous fit of $\pi^{\pm}$, $K^{\pm}$, p and $\bar{p}$ and the the variation of obtained parameters (T_{kin} and $\langle\beta\rangle$). The low p_T part of pion is affected by the resonance decays due to which the pion spectra are fitted above p_T > 0.5 GeV/c. It can be seen from Fig. 6 that $\langle\beta\rangle$ decreases from central to peripheral collisions, indicating a more rapid expansion in central collisions. In contrast to $\langle\beta\rangle$, T_{kin} increases from central to peripheral collisions. The comparison of these two parameters with other energy data is shown, revealing an inverse relationship and a two-dimensional anti-correlation with each other. This suggests that the fireball in central collisions is longer lived than in peripheral collisions.

4. Summary

We presented measurements of identified particles ($\pi^{\pm}$, $K^{\pm}$, p, and $\bar{p}$) at mid-rapidity ($|y| < 0.1$) in Au+Au collisions at $\sqrt{s_{NN}} = 54.4$ GeV using the STAR detector. The normalized yields of pions and kaons exhibit clear energy and centrality dependence. The proton yield peaks at $\sqrt{s_{NN}} = 7.7$ GeV, declines until 39 GeV, then experiences a slight increase up to 200 GeV. The proton yield at low energies is mainly attributed to baryon stopping and increasing energy favours the dominance of the pair production mechanism. The ratio of anti-particles to particles yields in Au+Au collisions at $\sqrt{s_{NN}} = 54.4$ GeV follow the trend observed in worldwide data. The kinetic freeze-out parameter T_{kin}, increases from central to peripheral collisions, while $\langle\beta\rangle$ decreases. At $\sqrt{s_{NN}} = 54.4$ GeV, there is a two-dimensional anti-correlation between T_{kin} and $\langle\beta\rangle$, which follows the trend observed for other BES energies at STAR.

5. Acknowledgement

Author acknowledges support from the DST Research project grant no. SR/MF/PS-02/2021-PU.

References

1. Krishna Rajagopal and Frank Wilczek, *The condensed matter physics of QCD*, (World Scientific, 2061-2151, 2001).
2. Bernard, C. and Burch, T. and DeTar, C. and Osborn, J. and Gottlieb, Steven and Gregory, E. B. and Toussaint, D. and Heller, U. M. and Sugar, R., *Phys. Rev. D* **71**, 034504 (2005).
3. Stephanov, M. and Rajagopal, K. and Shuryak, E., *Phys. Rev. Lett.* **81**, 4816-4819 (1998).
4. N. Tetradis, *Nuclear Physics A* **726**, 0375-9474 (2003).
5. STAR Collaboration (Adamczyk, L. *et al.*), *Phys. Rev. C* **96**, 044904 (2017).
6. STAR Collaboration (Abelev, B. I. *et al.*), *Phys. Rev. C* **79**, 034909 (2009).
7. STAR Collaboration (Adam, J. and Adamczyk *et al.*), *Phys. Rev. C* **101**, 024905 (2020).
8. E802 Collaboratio (Y. Akiba *et al.*), *Nucl. Phys. A* **610**, 139c (1996).
9. E802 Collaboration (L. Ahle *et al.*), *Phys. Rev. C* **57**, 466 (1998).

10. E866 Collaboration, E917 Collaboration (L. Ahle *et al.*), *Phys. Lett. B* **476**, 1 (2000).
11. E895 Collaboration (J. Klay *et al.*), *Phys. Rev. Lett.* **88**, 102301 (2002).
12. NA49 Collaboration (C. Alt *et al.*), *Phys. Rev. C* **77**, 024903 (2008).
13. ALICE Collaboration (B. Abelev *et al.*), *Phys. Rev. C* **88**, 044910 (2013).
14. X. Sun, H. Masui, A. M. Poskanzer, and A. Schmah, *Phys. Rev. C* ,**91**, 024903 (2015).
15. STAR Collaboration (L. Adamczyk *et al.*), *Phys. Rev. C* **93**, 014907 (2016).